The stabilization of a hypersonic boundary layer using local sections of porous coating

Xiaowen Wang and Xiaolin Zhong

Citation: Phys. Fluids **24**, 034105 (2012); doi: 10.1063/1.3694808
View online: http://dx.doi.org/10.1063/1.3694808
View Table of Contents: http://pof.aip.org/resource/1/PHFLE6/v24/i3
Published by the American Institute of Physics.

The stabilization of a hypersonic boundary layer using local sections of porous coating

Xiaowen Wang[a] and Xiaolin Zhong
Department of Mechanical and Aerospace Engineering, University of California at Los Angeles, Los Angeles, California 90095, USA

(Received 11 October 2011; accepted 23 February 2012; published online 21 March 2012)

The stabilization effect of porous coating on the hypersonic boundary layers over flat plates and cones has been studied by theoretical analyses, experiments, and numerical simulations. It was found that porous coating slightly destabilizes Mack's first mode whereas it significantly stabilizes Mack's second mode. In previous studies, porous coating covers either the entire flat plate or the surface around half the cone circumference. The effect of porous coating location on boundary-layer stabilization has not been considered. Furthermore, the destabilization of Mack's first mode has not been studied in detail. In this paper, the stabilization of a Mach 5.92 flat-plate boundary layer using local sections of porous coating is studied with the emphasis on the effect of porous coating location and the first-mode destabilization. Artificial disturbances corresponding to a single boundary-layer wave are introduced near the leading edge. A series of stability simulations are carried out by locally putting felt-metal porous coatings along the flat plate. It is found that disturbances are destabilized or stabilized when porous coating is located upstream or downstream of the synchronization point. For felt-metal porous coating, the destabilization of Mack's first mode is significant. The results suggest that an efficient way to stabilize hypersonic boundary-layer flows is to put porous coating downstream of the synchronization point. Finally, porous coating is used to stabilize the boundary layer disturbed by one blowing-suction actuator. [http://dx.doi.org/10.1063/1.3694808]

I. INTRODUCTION

The performance of hypersonic transportation vehicles and re-entry vehicles and the design of their thermal protection systems are significantly affected by the transition of boundary-layer flows over vehicle surfaces as turbulent boundary layers generate much higher surface friction and heating. Transition can have a first-order impact on lift, drag, stability, control, and heat transfer properties of the vehicles.[1] Transition control to maintain laminar boundary-layer flows or delay transition can result in lower drag, lower heat flux to surface, and higher fuel efficiency.

In order to predict and control boundary-layer transition, extensive studies have been carried out focusing on transition mechanisms.[2–4] It has been demonstrated that transition of external shear flows, including boundary layers, strongly depends on the amplitude of environmental disturbances. Figure 1 schematically shows transition paths of external shear flows. For small amplitude disturbances, the transition of a boundary layer over a smooth surface generally consists of the following three stages: (1) Receptivity process during which environmental disturbances enter the boundary layer and excite boundary-layer waves. (2) Modal growth of unstable boundary-layer waves which can be obtained by solving the eigen-problem of the homogeneous linearized stability equations. (3) Breakdown to turbulence caused by nonlinear secondary instabilities and three-dimensional effects when the unstable waves reach a certain amplitude. This three-stage-transition mechanism is path 1 as shown in Fig. 1. With the disturbance amplitude increasing, transient growth, arising through

[a]E-mail: xiaowen@seas.ucla.edu.

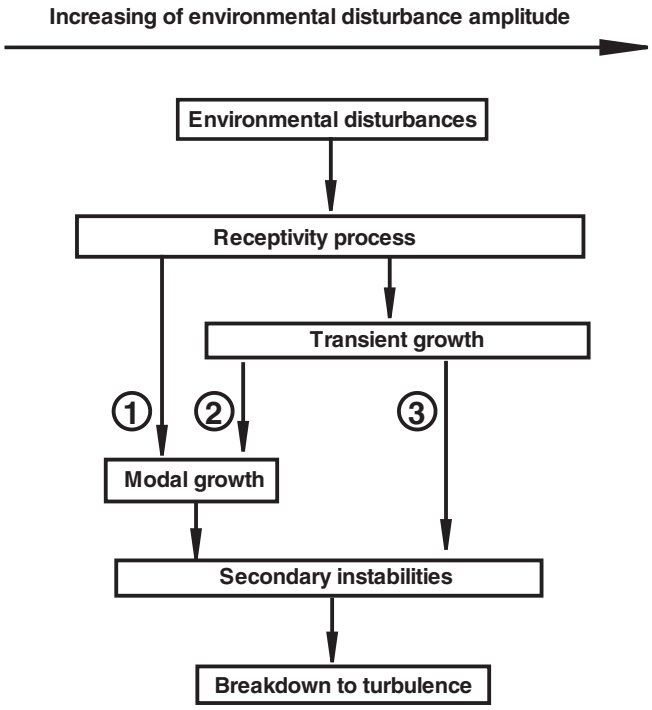

FIG. 1. Transition paths of external shear flows with respect to the amplitude of environmental disturbance (Reshotko[2]).

the non-orthogonal nature of the Orr-Sommerfeld eigenfunctions and the Squire eigenfunctions, becomes important. Weak transient growth provides a higher initial amplitude for modal growth (path 2) whereas strong transient growth can lead to secondary instabilities and breakdown to turbulence right after the receptivity process (path 3). Porous coatings are used to stabilize the boundary layer by attenuating modal growth.

For the stability of hypersonic boundary layers, different terminologies for boundary-layer waves have been used in the literature by Mack,[5] Ma and Zhong,[6] and Tumin.[7] In Tumin's theoretical analyses, the first mode, second mode, etc. of Mack are called mode S. The Mode I, Mode II, etc. of Ma and Zhong are called mode F. Mathematically, the terminologies used by Tumin are more clear and recommended for both mathematical analyses and interpretation of direct numerical simulations.[8] Mode S and mode F are given the names because they are tuned to slow and fast acoustic waves, respectively, in the limit of small Reynolds numbers. Mode F is generally stable whereas mode S is unstable in the region bounded by a neutral curve. Therefore, mode S is more relevant in the three-stage transition. Mack's first mode may be inviscidly unstable at sufficiently high Mach numbers because compressible boundary-layer profiles contain an inflection point, but its instability is most important at finite Reynolds numbers. For boundary layers over adiabatic surfaces, Mack's second mode exists when flow Mach numbers are above 2.2 and becomes important when Mach numbers are larger than 4. According to the three-stage-transition mechanism, stabilization of Mack's first and second modes are critical to transition control.

Passive control of boundary-layer transition by using porous coating to stabilize hypersonic boundary layers over flat plates and cones has been studied using theoretical analyses, experiments, and numerical simulations.[9–15] Fedorov *et al.*[9] theoretically analyzed the second-mode stability of a hypersonic boundary layer over a flat plate covered by an ultrasonically absorptive coating (UAC). They found that the second mode growth was massively reduced because the porous layer absorbed some energy from the disturbance. Rasheed *et al.*[10] experimentally studied the stability of a Mach 5 boundary layer on a sharp 5.06° half-angle cone at zero angle of attack. The cone had a smooth surface around half the cone circumference and an UAC porous surface on the other half. Their experiments indicated that the porous surface was highly effective in stabilizing the second

mode and delaying transition when the pore size was significantly smaller than the disturbance wavelength. The experiments carried out by Fedorov and co-workers[11–13] also showed that porous coating strongly stabilized the second mode and marginally destabilized the first mode. Chokani *et al.*[14] studied the nonlinear aspects of the second-mode stabilization for a regular microstructure using bispectral analysis. The spectral measurements showed that the harmonic resonance of the second mode is completely absent on the porous surface, and the first mode is moderately destabilized. Maslov[15] experimentally studied the stabilization of a hypersonic boundary layer by microstructural porous coating. In his experiments, both regular structure UAC and random felt-metal UAC are used. The results confirmed that porous coating strongly stabilizes the second mode and marginally destabilizes the first mode. Compared with regular structure UAC, felt-metal UAC is much stronger in first mode destabilization, with the peak amplitude of the first mode increasing around 70%.

Recently, more researchers have carried out studies in this field.[16–19] Fedorov and Malmuth[20] conducted parametric studies of the regular porous coating performance for Mach 7 and 10 freestream conditions. They found that the porous coating performance strongly increases with porosity. Egorov *et al.*[21] studied the effect of porous coating on stability and receptivity of a Mach 6 flat-plate boundary layer by two-dimensional numerical simulation using a second-order total variation diminishing (TVD) scheme. They found that a porous coating of regular porosity effectively diminishes the second mode growth rate, while weakly affecting acoustic waves. Sandham and Lüdeke[22] numerically studied Mack mode instability of a Mach 6 boundary layer over a porous surface. It was shown that the detailed surface structure is not as important as the overall porosity. Stephen and Michael[23] theoretically considered the effect of a porous wall on Mack's first mode for a hypersonic boundary layer on a sharp slender cone. They found that the porous wall significantly destabilized the non-axisymmetric modes. Lukashevich *et al.*[24] studied the effect of porous coating thickness on the stabilization of high-speed boundary layers. They demonstrated that the stalibization effect essentially depends on the UAC thickness and then figured out the optimal thickness. In summary, previous results consistently showed that porous coating significantly stabilizes Mack's second mode and moderately destabilizes Mack's first mode. Therefore, local stabilization of Mack's second mode is stronger than local destabilization of Mack's first mode. At a fixed location, porous coating reduces the overall disturbances.

In previous studies, porous coating covers either the entire flat plate or the surface around half the cone circumference. The effect of porous coating location on boundary-layer stabilization has not been studied. In fact, placement of porous coating can affect the efficiency of boundary-layer stabilization. If Mack's first mode propagates from upstream to downstream, it will spatially develop into Mack's second mode. In this case, the upstream first-mode destabilization is very important: it leads to a stronger Mack's second mode where porous coating now has to stabilize the much stronger second mode. Overall, the upstream first-mode destabilization decreases the efficiency of boundary-layer stabilization. A straightforward way to avoid first-mode destabilization is to put porous coating only where Mack's second mode is dominant. In a previous numerical study, Wang *et al.*[25] showed that the synchronization point of mode F and mode S plays an important role in the excitation of mode S. The results indicate that the synchronization point might be the right location to start putting porous coating.

In this paper, the stabilization of a Mach 5.92 boundary layer over a flat plate using local sections of porous coating is studied by a combination of direct numerical simulation (DNS) and linear stability theory (LST), with the emphasis on the effect of porous coating location and the first-mode destabilization. At first, the role of the synchronization point on boundary-layer stabilization is investigated by a series of stability simulations. The stability simulations consist of two steps: (1) Periodic disturbances corresponding to mode S or mode F are superimposed on steady base flow at a cross section of the boundary layer to show spatial development of the wave. While it is hard to generate pure mode S or mode F in experiment, numerical simulations have the advantage of using pure mode to simplify the problem. (2) Local sections of porous coating are used downstream of the superimposed wave to investigate its effect on boundary-layer instability. For superimposed mode S, six sections of porous coating are considered, with three of them being located upstream of the synchronization point. For superimposed mode F, only the three sections of porous coating

located upstream of the synchronization point are considered. Numerical results are interpreted by comparing with LST analyses. Porous coating is then used to stabilize the boundary layer disturbed by one blowing-suction actuator.

II. GOVERNING EQUATIONS AND FLOW CONDITIONS

The Mach 5.92 boundary layer over a flat plate, as schematically shown in Fig. 2, is considered. In the figure, the streamwise propagating disturbances in the boundary layer are excited by either superimposed mode S/mode F or the blowing-suction actuator. The flow is assumed to be thermally and calorically perfect. The governing equations are the compressible Navier-Stokes equations, i.e.,

$$\frac{\partial \vec{U}^*}{\partial t^*} + \frac{\partial}{\partial x_1^*}(\vec{F}_{1i}^* + \vec{F}_{1v}^*) + \frac{\partial}{\partial x_2^*}(\vec{F}_{2i}^* + \vec{F}_{2v}^*) = 0\,, \tag{1}$$

where $\vec{U}^*$ is a column vector containing the conservative variables of mass, momentum, and energy, i.e.,

$$\vec{U}^* = \{\rho^*, \rho^* u_1^*, \rho^* u_2^*, e^*\}^{\mathrm{T}}\,. \tag{2}$$

The flux vectors in Eq. (1) are divided into their inviscid and viscous components because the two components are discretized with different schemes. The components, $\vec{F}_{1i}^*$ and $\vec{F}_{2i}^*$, are inviscid flux whereas $\vec{F}_{1v}^*$ and $\vec{F}_{2v}^*$ are viscous flux components.

In Eq. (1), there are four equations and five unknown variables equation of state is needed to solve the governing equations. Under the perfect gas assumption, pressure and energy are given by

$$p^* = \rho^* R^* T^*\,, \tag{3}$$

$$e^* = \rho^* c_v^* T^* + \frac{\rho^*}{2}(u_1^{*2} + u_2^{*2})\,, \tag{4}$$

where c_v^* is the specific heat at constant volume. Refer to our recent paper[26] for details of governing equations and numerical methods.

In this paper, the superscript "*" represents dimensional variables. Numerical simulations are carried out for dimensional variables. In the analyses of numerical results, the dimensional flow variables are non-dimensionalized by freestream parameters. Specifically, density, temperature,

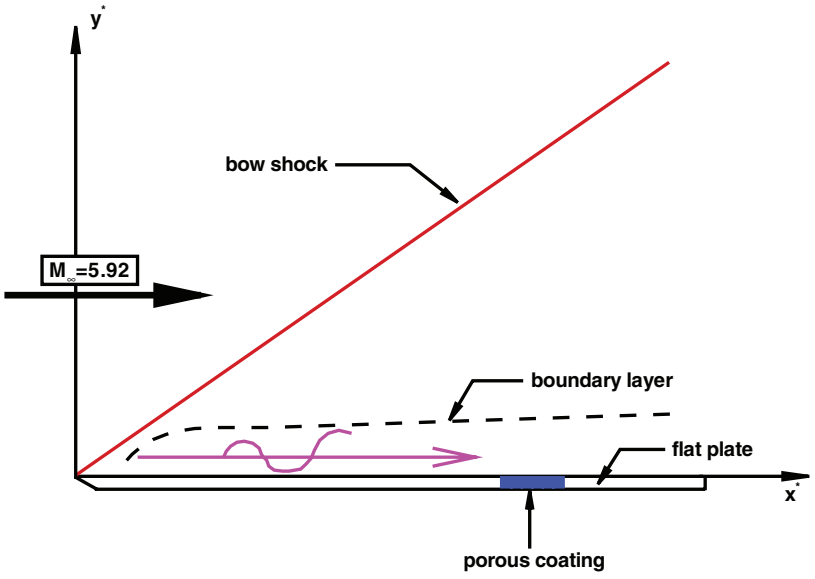

FIG. 2. A schematic of the stabilization of a Mach 5.92 flat-plate boundary layer using porous coating.

velocity, and pressure are non-dimensionalized by ρ^*_∞, T^*_∞, u^*_∞, and $\rho^*_\infty u^{*2}_\infty$. Furthermore, x^*_1 is non-dimensionalized by unit length in meter, whereas x^*_2 is non-dimensionalized by the local boundary layer thickness, $\sqrt{\mu^*_\infty x^*_1/\rho^*_\infty u^*_\infty}$. Referring to the coordinate system shown in Fig. 2, x^*_1 and x^*_2 are x^* and y^*, respectively. The two variables, u^*_1 and u^*_2, are velocities in the streamwise and wall-normal directions.

Freestream flow conditions are the same as those of Maslov *et al.*'s experiment,[27] i.e.,

$$\begin{aligned} &M_\infty = 5.92, && T^*_\infty = 48.69\ \text{K},\\ &p^*_\infty = 742.76\ \text{Pa}, && Pr = 0.72,\\ &f^* = 100\ \text{kHz}, && F = 53.03 \times 10^{-6},\\ &Re^*_\infty = 14.12 \times 10^6/\text{m}, \end{aligned}$$

where Re^*_∞ is the unit Reynolds number defined as

$$Re^*_\infty = \frac{\rho^*_\infty u^*_\infty}{\mu^*_\infty}. \tag{5}$$

One may notice that, in Maslov *et al.*'s experiment,[27] $Re^*_\infty = 13 \times 10^6/\text{m}$. The difference of unit Reynolds number comes from the calculation of freestream viscosity. In our numerical simulations, viscosity is calculated by Sutherland's law. In the freestream, Sutherland's law is not valid for such a low temperature as $T^*_\infty = 48.69$ K, which leads to a smaller viscosity and a higher unit Reynolds number. Since numerical simulations are carried out for flow after the shock, where temperature is much higher than freestream temperature, it is still valid to use Sutherland's law. In other words, the difference of unit Reynolds number has no effect on the dimensional numerical simulation. It only plays a role in the analyses of numerical results.

In both steady and unsteady simulations, inlet conditions are specified. High-order extrapolation is used for outlet conditions because the flow is hypersonic at the exit except a small region near the flat plate. Flow variables behind the shock are solved by combining Rankine-Hugoniot relations across the shock and a characteristic compatibility relation coming from downstream flow. For the steady base flow simulation the wall is adiabatic, and the physical boundary condition for velocity on the flat plate is the no-slip condition. In stability simulations, special treatment of wall boundary conditions is needed. When disturbances are introduced, temperature perturbation is set to zero, which is a standard boundary condition for theoretical and numerical studies of high frequency disturbances. Meanwhile, the no-slip condition is applied on the flat plate except in the blowing-suction region and porous coating region.

The same flow has been used in numerical simulations of boundary-layer stabilities.[26,28] The dimensional streamwise coordinate x^*, as shown in Fig. 2, can be converted to local Reynolds number by

$$Re_x = Re^*_\infty x^*\,. \tag{6}$$

In LST analyses of boundary layer flows, the Reynolds number based on the local length scale of boundary layer thickness, L^*, is generally used and is expressed as

$$R = \frac{\rho^*_\infty u^*_\infty L^*}{\mu^*_\infty}, \quad L^* = \sqrt{\frac{\mu^*_\infty x^*}{\rho^*_\infty u^*_\infty}}\,. \tag{7}$$

Hence, the relation between R and local Reynolds number Re_x is given by

$$R = \sqrt{Re_x}\,. \tag{8}$$

III. POROUS COATING AND BLOWING-SUCTION ACTUATOR MODELS

At step 1 of the stability simulations, disturbances corresponding to a specific boundary layer wave at a frequency of 100 kHz are introduced at a cross section of the boundary layer. The

disturbances are a combination of velocity, pressure, and temperature oscillations, which can be expressed as

$$\begin{Bmatrix} \tilde{u}^* \\ \tilde{v}^* \\ \tilde{w}^* \\ \tilde{p}^* \\ \tilde{T}^* \end{Bmatrix} = \epsilon_1 \begin{Bmatrix} \hat{u}^*(y^*) \\ \hat{v}^*(y^*) \\ \hat{w}^*(y^*) \\ \hat{p}^*(y^*) \\ \hat{T}^*(y^*) \end{Bmatrix} \sin(\omega^* t^*) \,, \tag{9}$$

where ϵ_1 is a small dimensionless parameter representing the amplitude of disturbances. The vector, $\{\hat{u}^*(y^*),\ \hat{v}^*(y^*),\ \hat{w}^*(y^*),\ \hat{p}^*(y^*),\ \hat{T}^*(y^*)\}^{\mathrm{T}}$, represents the eigenfunctions of mode S or mode F, which is obtained from LST analyses. The profiles of disturbances are normalized by the pressure perturbation on the wall. In the above equation, ω^* is the circular frequency of the disturbances, which is related to the frequency by

$$\omega^* = 2\pi f^* \,. \tag{10}$$

The circular frequency, ω^*, and the frequency, f^*, are non-dimensionalized according to

$$\omega = \frac{\omega^* L^*}{u^*_\infty} \,, \tag{11}$$

$$F = \frac{2\pi f^* \mu^*_\infty}{\rho^*_\infty u^{*2}_\infty} = \frac{\omega^* \mu^*_\infty}{\rho^*_\infty u^{*2}_\infty} \,. \tag{12}$$

With the definitions of Reynolds number R and the dimensionless frequency F, the dimensionless circular frequency can also be expressed as

$$\omega = RF \,. \tag{13}$$

If F is a constant in Eq. (13), $\omega \propto (x^*)^{1/2}$. Therefore, plots versus ω are also plots versus distance if the frequency is fixed.

At step 2 of stability simulations, felt-metal porous coating similar to that of Fedorov *et al.*[11] is used. Porous coating is modeled by wall blowing-suction relating to pressure perturbations. The wall-normal velocity disturbance induced by porous coating is

$$v' = A_y p' \,. \tag{14}$$

The porous coating admittance, A_y, is defined as

$$A_y = -\frac{\phi}{Z_0} \tanh(\Lambda h) \,. \tag{15}$$

In the above equation, ϕ is porosity and h is the porous-layer thickness non-dimensionalized by the local length scale of the boundary layer thickness,

$$h = \frac{h^*}{L^*} = h^* \sqrt{\frac{\rho^*_\infty u^*_\infty}{\mu^*_\infty x^*}} \,. \tag{16}$$

According to Allard and Champoux's theoretical analyses,[29] the empirical equations for porous coating characteristic impedance (Z_0) and propagation constant (Λ) are

$$Z_0 = \frac{\rho_w}{M_e} \sqrt{\frac{T_w \tilde{\rho}}{\tilde{C}}} \,, \tag{17}$$

$$\Lambda = \frac{i\omega M_e}{\sqrt{T_w}} \sqrt{\tilde{\rho}\tilde{C}} \,, \tag{18}$$

where ρ_w and T_w are the local dimensionless density and temperature on the porous coating surface. The edge Mach number (M_e) is defined right after the shock. The dynamic density ($\tilde{\rho}$) and bulk modulus ($\tilde{C}$) are calculated from the following equations:

$$\tilde{\rho} = a_\infty \left[1 + \frac{g(\lambda_1)}{\lambda_1} \right] , \tag{19}$$

$$\tilde{C} = \gamma - \frac{\gamma - 1}{1 + \frac{g(\lambda_2)}{\lambda_2}} . \tag{20}$$

In these two equations, λ_1, λ_2, and the function $g(\lambda)$ are defined as

$$g(\lambda) = \sqrt{1 + \frac{4 a_\infty \mu_w^* \lambda}{\sigma^* \phi r_p^{*2}}} , \tag{21}$$

$$\lambda_1 = \frac{i a_\infty \rho_w^* \omega^*}{\phi \sigma^*} , \tag{22}$$

$$\lambda_2 = 4 \mathrm{Pr} \lambda_1 , \tag{23}$$

where a_∞ is the tortuosity, $\sigma*$ is the flow resistivity, and r_p^* is the characteristic pore size. These parameters are determined by the porous coating. In the porous coating model, the local dimensionless variables (v, p, T_w, ρ_w, ω) are non-dimensionalized by the corresponding variables right after the shock, (u_e^*, $\rho_e^* u_e^{*2}$, T_e^*, ρ_e^*, $\sqrt{\mu_e^* x^* / \rho_e^* u_e^*}/u_e^*$).

With the definitions of characteristic impedance and propagation constant, porous coating admittance is generally a complex number. Velocity perturbation calculated by Eq. (14) is also a complex number. However, only the real part of the velocity perturbation can be imposed in numerical simulations. The velocity perturbation used in DNS is written relating to the instantaneous pressure perturbation ($p(t*)$) as

$$v(t^*) = \mathrm{Real}(A_y) p(t^*) + \mathrm{Imag}(A_y) \frac{dp(t^*)}{\omega^* dt^*} , \tag{24}$$

where "Real(A_y)" and "Imag(A_y)" represent the real and imaginary parts of porous coating admittance, respectively.

Finally, porous coating is used to stabilize the boundary layer disturbed by one blowing-suction actuator. The mass flux oscillation on the flat plate within the blowing-suction region can be written as

$$(\rho^* v^*)' = q_0^* \epsilon_2 \beta(l) \sin \omega^* t^* , \tag{25}$$

where q_0^* is a constant locally defined at the leading edge of the blowing-suction actuator and ϵ_2 is a small dimensionless parameter representing the amplitude of the mass flux oscillation. The function $\beta(l)$ is the profile function defined within the forcing region as

$$\beta(l) = \begin{cases} 20.25 l^5 - 35.4375 l^4 + 15.1875 l^2 & \text{if } l \le 1 \\ -20.25(2-l)^5 + 35.4375(2-l)^4 - 15.1875(2-l)^2 & \text{if } l \ge 1 \end{cases} . \tag{26}$$

The variable l is a dimensionless coordinate defined within the blowing-suction region,

$$l = \frac{2(x^* - x_i^*)}{x_e^* - x_i^*} , \tag{27}$$

where x_i^* and x_e^* are the coordinates of the leading and trailing edges of the blowing-suction actuator. Due to the anti-symmetric property of the 5th-order-polynomial profile function within the blowing-suction region, the net mass flux introduced to the boundary layer is zero at any instant.

IV. SPATIAL DEVELOPMENT OF MODE S AND MODE F

At step 1 of the stability simulations, periodic disturbances corresponding to mode F or mode S are superimposed on the steady base flow at a cross section of the boundary layer to show spatial development of the wave. The steady base flow over the flat plate is simulated by solving the two-dimensional compressible Navier-Stokes equations with a combination of a fifth-order shock-fitting finite difference method and a second-order TVD scheme. The stability characteristics of the hypersonic boundary layer are analyzed using LST. In this paper, only the most important LST results are discussed. More details of LST analyses and the steady base flow simulation can be found in Wang and Zhong's paper.[26]

In a spatial stability problem, the complex wave number α can be expressed as

$$\alpha = \alpha_r + i\alpha_i, \tag{28}$$

where $-\alpha_i$ is the local growth rate. A boundary-layer wave is unstable when $\alpha_i < 0$ and stable when $\alpha_i > 0$. The points where $\alpha_i = 0$ are called neutral points of a boundary-layer wave. A wave is generally unstable only in certain domains bounded by neutral points. The real part of α is the local wave number which can be used to define the local phase velocity:

$$a = \frac{\omega}{\alpha_r}. \tag{29}$$

Both wave number and phase velocity can be used to identify a boundary-layer wave.

Figure 3 shows the dimensionless phase velocities of boundary-layer waves at two locations, $x^* = 0.159$ m and $x^* = 0.189$ m ($R = 1437.71$ and 1567.48), as a function of the dimensionless circular frequency. In this figure, the frequency of boundary-layer waves is changing. The three horizontal dashed lines represent the dimensionless phase velocities of fast acoustic waves ($a = 1 + M_\infty^{-1}$), entropy and vorticity waves ($a = 1$), and slow acoustic waves ($a = 1 - M_\infty^{-1}$), respectively. Theoretically, the phase velocities of fast and slow acoustic waves should be calculated with the Mach number behind the shock. However, the Mach number behind the shock is not a constant in the computational domain.[26] For convenience, the freestream Mach number is used in the current paper. The excellent agreement of the phase velocities at different locations indicates that the phase velocity is approximately a function of dimensionless circular frequency only. The figure

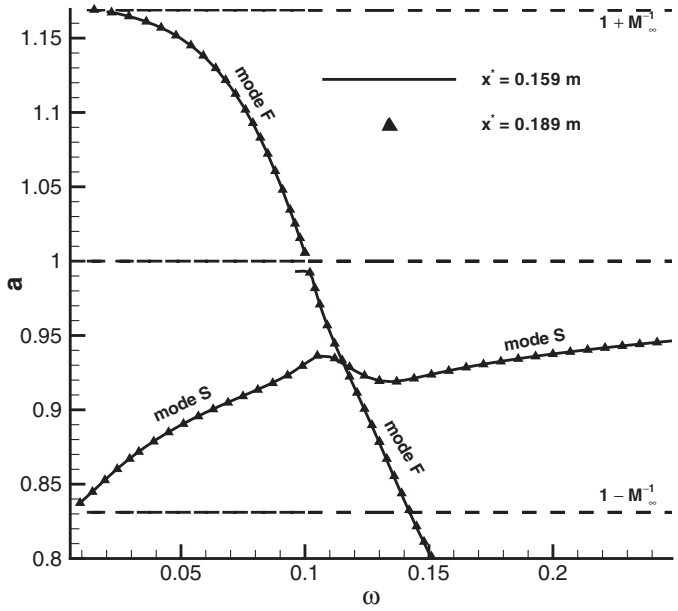

FIG. 3. Dimensionless phase velocities of mode S and mode F at two different locations versus dimensionless circular frequency.

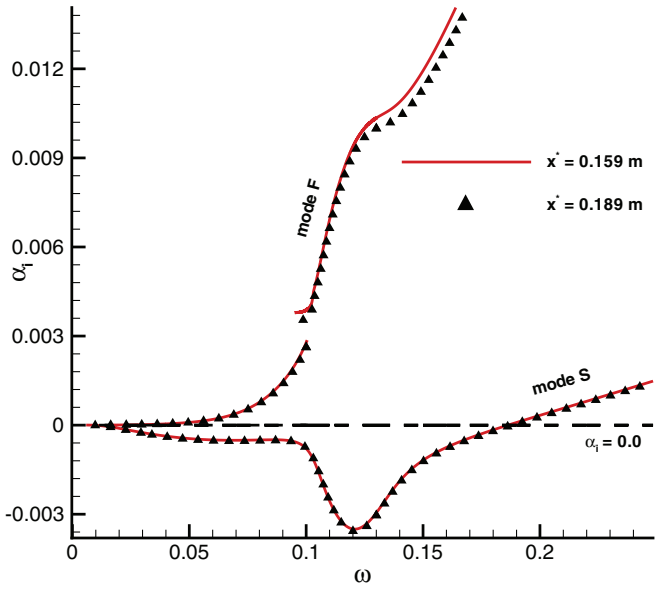

FIG. 4. Growth rates of mode S and mode F at two different locations versus dimensionless circular frequency.

clearly shows that, in the limit of small dimensionless circular frequency, mode F and mode S are tuned to fast and slow acoustic waves, respectively. As ω increases, the phase velocity of mode F decreases. When mode F passes the continuous entropy and vorticity waves near $\omega = 0.1$, there exists a jump in phase velocity, caused by the resonance between mode F and entropy/vorticity waves. The figure also shows that mode S synchronizes with mode F at the point where $\omega_s = 0.11563$ and $a_s = 0.93076$. At the synchronization point, dimensionless phase velocities of mode S and mode F are identical. Location of the synchronization point in the x^* coordinate for a given dimensionless frequency can be calculated using the following formula:

$$x_s^* = \frac{(\omega_s/F)^2}{Re_\infty^*}. \tag{30}$$

Figure 4 shows the growth rates of mode S and mode F at the same set of locations as a function of the dimensionless circular frequency. The horizontal dashed line stands for the neutral waves ($\alpha_i = 0$). In Fig. 4, the growth rates of mode S at the two locations agree well and they are approximately functions of dimensionless circular frequency only. Mode S is unstable in the region from $\omega_I = 0.01827$ to $\omega_{II} = 0.18465$. The parameters, ω_I and ω_{II}, are called the Branch I and Branch II neutral points of mode S. Mode S is stable upstream of the Branch I neutral point and downstream of the Branch II neutral point. The locations of the Branch I and Branch II neutral points in the x^* coordinate can be calculated from

$$x_I^* = \frac{(\omega_I/F)^2}{Re_\infty^*}, \tag{31}$$

$$x_{II}^* = \frac{(\omega_{II}/F)^2}{Re_\infty^*}. \tag{32}$$

Periodic disturbances corresponding to mode S or mode F at a frequency of 100 kHz are superimposed on the steady base flow at a cross section of the boundary layer at $x^* = 69.00$ mm ($R = 987.24$). The frequency of superimposed disturbances is chosen based on the following two reasons. First, porous coating characteristic impedance and propagation constant, defined by Eqs. (17) and (18), are frequency dependent. It is hard to simulate the response of porous coating to multi-frequency disturbances. Therefore, in Egorov *et al.*'s numerical simulations,[21] only the

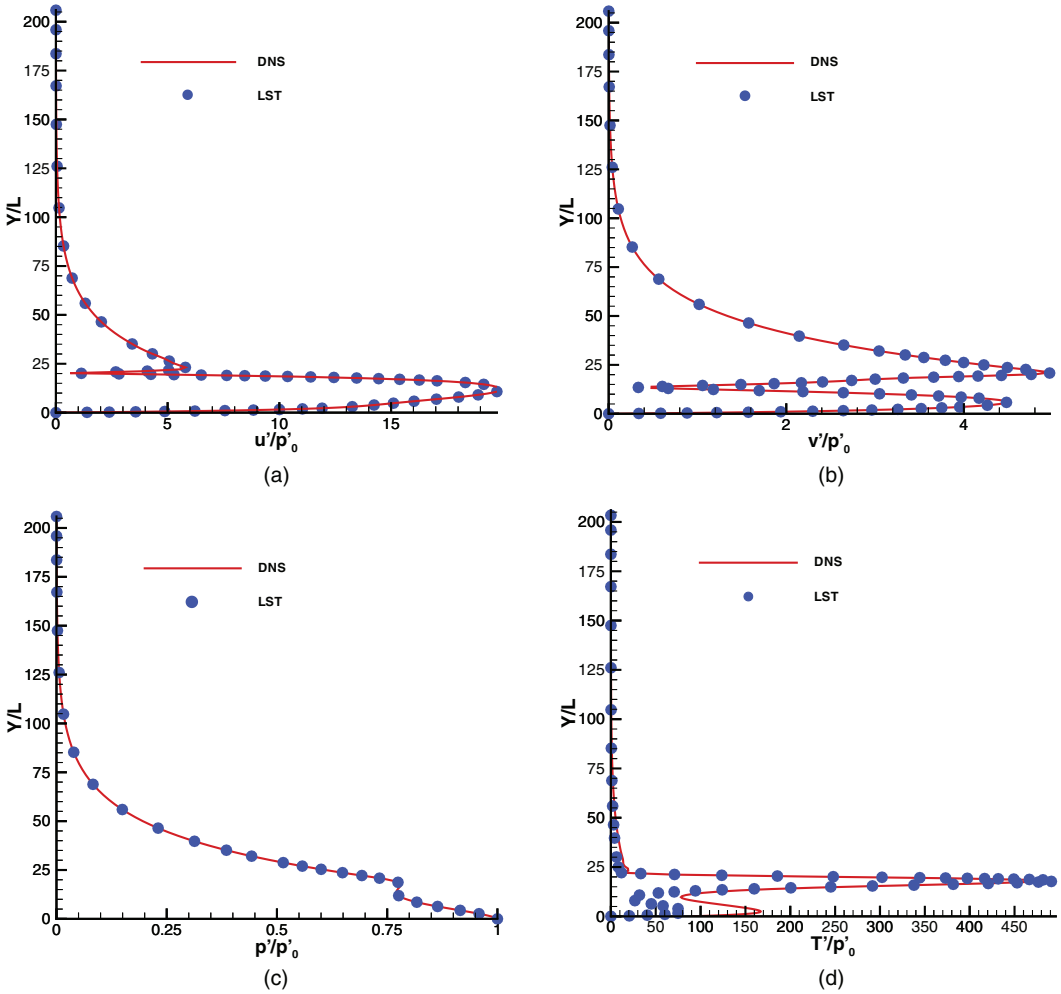

FIG. 5. Comparisons of superimposed mode S with the eigenfunctions of mode S obtained from LST: (a) streamwise velocity, (b) wall-normal velocity, (c) pressure, and (d) temperature.

disturbance at a single frequency ($F = 1.3 \times 10^{-4}$) is considered. Second, the numerical simulations of Wang and Zhong[26] showed that the Mach 5.92 flat-plate boundary layer has a strong response to disturbances at the frequency of 100 kHz. For the boundary-layer waves considered in the current paper ($f^* = 100$ kHz, $F = 53.03 \times 10^{-6}$), the synchronization point and the two neutral points in the x^* coordinate are, respectively, located at 0.33184 m, 8.40310×10^{-3} m, and 0.84622 m.

The computational domain for the stability simulation starts at $x^* = 69.00$ mm ($R = 987.24$) and ends at $x^* = 0.8590$ m ($R = 3483.32$). The parameters of disturbance amplitude, ϵ_1 in Eq. (9), are assigned to mode S and mode F as 1.0×10^{-8} and 1.0×10^{-6}, respectively. These two values are small enough to preserve the linear properties of the disturbances. Figure 5 compares superimposed mode S with the eigenfunctions of mode S obtained from LST. Similar comparisons of mode F are shown in Fig. 6. In these two figures, the eigenfunctions of mode S and mode F are obtained from LST at $x^* = 69.00$ mm with the parallel flow assumption. Both superimposed disturbances and the eigenfunctions are normalized by the corresponding pressure disturbance on the wall. The good agreements of velocity and pressure profiles indicate that the disturbances superimposed on the steady base flow are exactly mode S or mode F. The discrepancy between temperature profiles near the wall ($y/L < 10$), as shown in Figs. 5(d) and 6(d), is caused by the nonparallel flow effect. In the stability simulations, temperature profiles of superimposed disturbances are calculated using pressure and density eigenfunctions of corresponding waves obtained from LST, together with mean

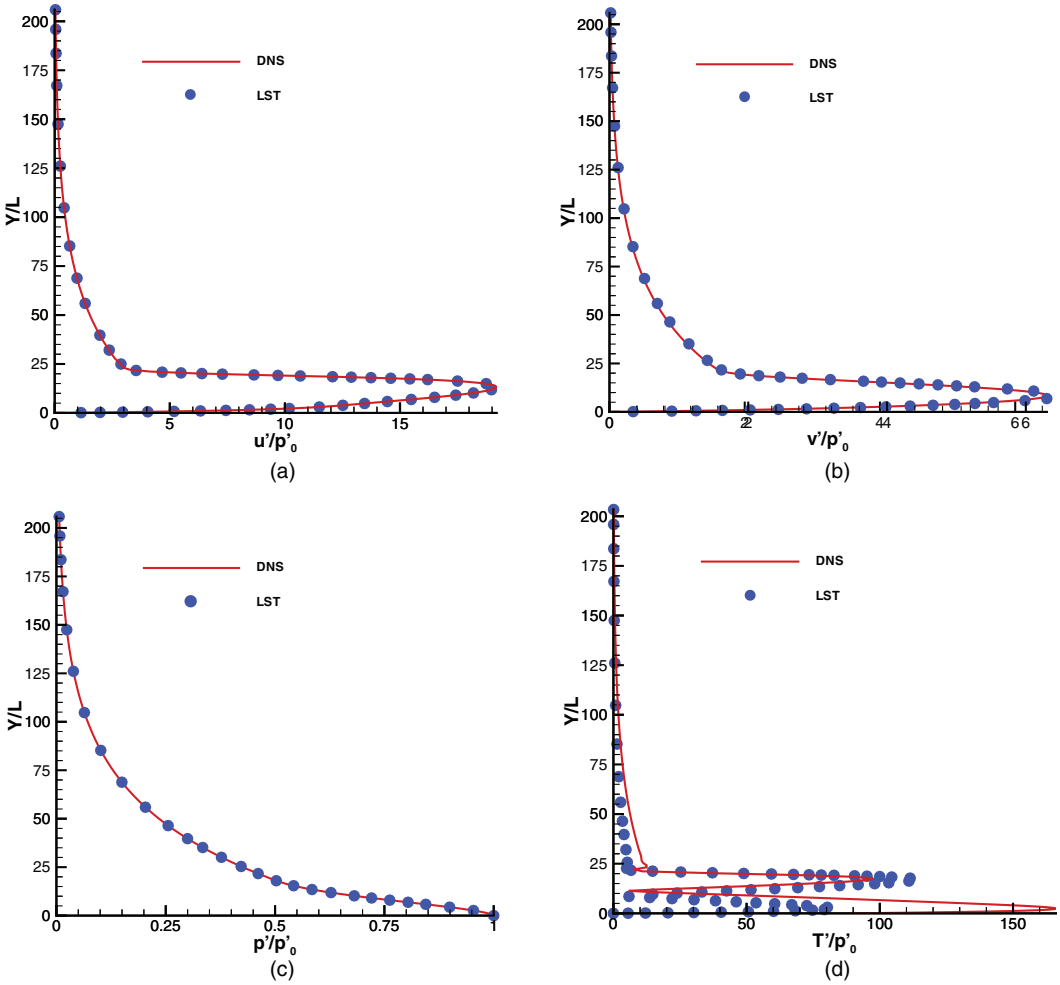

FIG. 6. Comparisons of superimposed mode F with the eigenfunctions of mode F obtained from LST: (a) streamwise velocity, (b) wall-normal velocity, (c) pressure, and (d) temperature.

flow temperature, pressure, and density obtained from DNS, i.e.,

$$\tilde{T}^* = T_0^*\left(\frac{\tilde{p}^*}{p_0^*} - \frac{\tilde{\rho}^*}{\rho_0^*}\right), \tag{33}$$

where T_0^*, p_0^*, and ρ_0^* are mean flow temperature, pressure, and density. $\tilde{p}^*$ and $\tilde{\rho}^*$ are pressure and density eigenfunctions. Nonparallel flow effects are included in the mean flow simulation.

Figure 7 shows the spatial development of superimposed mode S and mode F. In this figure, the spatial development of superimposed mode F with an amplitude parameter of 1.0×10^{-8} is also plotted. The symbols represent one hundredth of the exact pressure perturbation related to superimposing mode F with the amplitude parameter set as 1.0×10^{-6}. It is clearly shown that the spatial development of mode F with different amplitudes has the same profile. A one hundred times difference in superimposed disturbance amplitude leads to a 100 times amplitude difference in downstream pressure perturbation, which demonstrates the linear properties of the superimposed mode F. When mode S is superimposed at $x^* = 69.00$ mm ($R = 987.24$) it grows dramatically where the peak of pressure perturbation amplitude is around $x^* = 0.8$ m ($R = 3361.57$). The scenario of mode F is quite different from that of mode S. After a transient process, pressure perturbation amplitude of mode F decreases because mode F is a stable wave. The lowest pressure perturbation

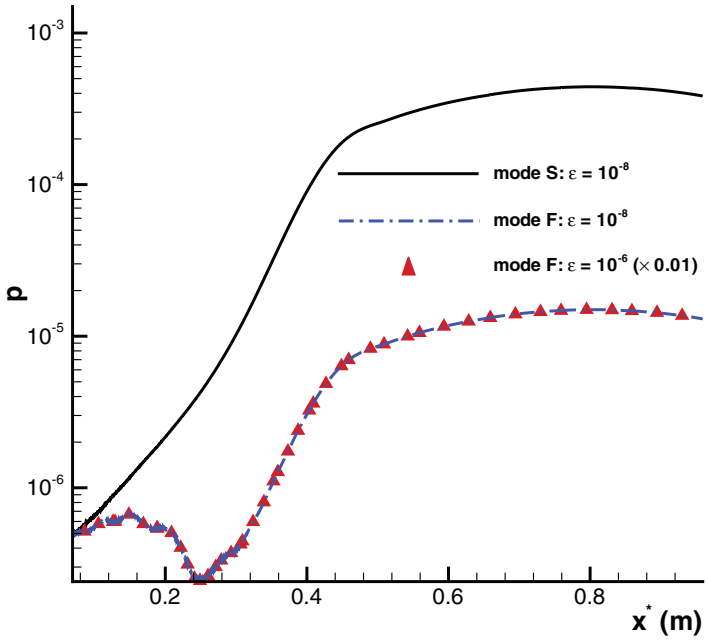

FIG. 7. Spatial development of superimposed mode S and mode F.

amplitude of mode F is observed at around $x^* = 0.24$ m ($R = 1841.21$). After that, the wave grows similar to mode S with the amplitude peak around $x^* = 0.8$ m ($R = 3361.57$).

In order to quantitatively study the spatial development of superimposed waves, a local wave number (α_r) and a local growth rate (α_i) related to pressure perturbation along the flat plate are calculated,

$$\alpha_r = L^* \frac{d\phi'}{dx^*}, \tag{34}$$

$$\alpha_i = -\frac{L^*}{|p'|} \frac{d|p'|}{dx^*}, \tag{35}$$

where L^* is the length scale of the local boundary layer thickness as defined by Eq. (7). $|p'|$ and ϕ' are pressure perturbation amplitude and phase angle, respectively. The parameters α_r and α_i represent the true wave number and growth rate only if the perturbation is dominated by a single wave. Otherwise, the disturbance needs to be decomposed to check properties of a specific wave. For example, Tumin, Wang, and Zhong[30] decomposed the disturbance at a location just downstream of the blowing-suction actuator with a biorthogonal eigenfunction system where mode F, mode S, and continuous waves coexisted and none of them was dominant.

Since only one boundary layer wave is superimposed in the stability simulations, the superimposed wave is dominant in the boundary layer. In this case, Eqs. (34) and (35) can be used to check the properties of the superimposed wave. Figure 8 compares the growth rate calculated from the stability simulations with that obtained from LST for superimposed mode S and mode F. For mode S, the growth rate from the stability simulation has a good agreement with that of LST in the region $\omega = 0.11$ to $\omega = 0.13$. When ω is larger than 0.13, the growth rate from the stability simulation is larger than that of LST, i.e., mode S obtained by the stability simulation becomes more stable than that predicted by LST. However, when ω is smaller than 0.11, mode S obtained by the stability simulation becomes more unstable than that predicted by LST. This is due to the growth rate from the stability simulation being smaller than that predicted by LST.

For mode F, the figure shows that the growth rate of the stability simulation initially follows that of LST. However, it approaches that of mode S near the synchronization point, which indicates that

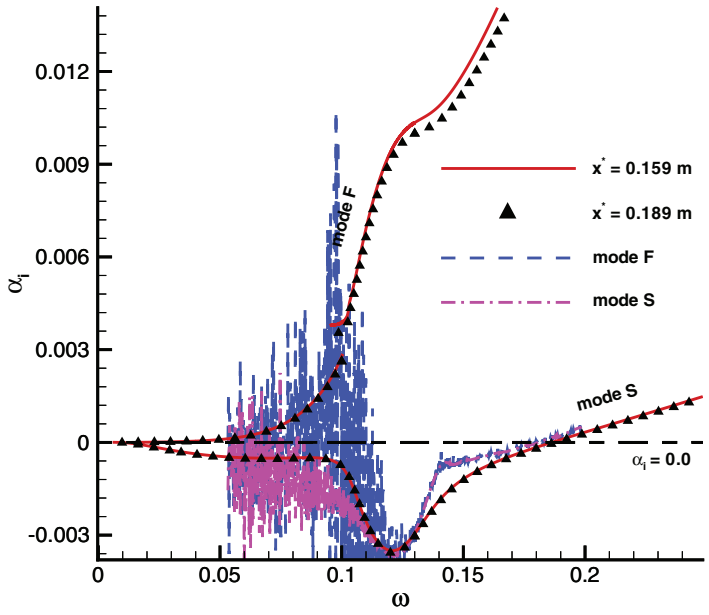

FIG. 8. Comparison of the growth rate calculated from stability simulations with that obtained from LST for superimposed mode S and mode F.

mode F mainly converts to mode S near the synchronization point. The existence of another mode F is possible after the branching of mode S and mode F, but it seems to have a much smaller amplitude than that of mode S in this case. After the synchronization point, the growth rate of the stability simulation has a good agreement with that of mode S. The discrepancy between the growth rates of mode S calculated from the stability simulation and LST, when ω is larger than 0.13 or smaller than 0.11, is mainly caused by nonparallel flow effects which have been theoretically interpreted by Tumin, Wang, and Zhong.[31] Nonparallel flow effects stabilize Mack's second mode and destabilize Mack's first mode.

Figure 9 compares the phase velocity calculated from the stability simulations with that obtained from LST for the superimposed mode S and mode F. For mode S, the phase velocity from the stability simulation has a good agreement with that of LST. It is clearly shown that the phase velocity of mode F has strong oscillations around $x^* = 0.24$ m ($R = 1841.21$), where mode F is resonant with vorticity and entropy waves. This resonance leads to initial growth of mode F around $x^* = 0.24$ m ($R = 1841.21$). After $x^* = 0.32$ m ($R = 2126.04$), the phase velocity of mode F approaches that of mode S, which indicates that mode F converts to mode S. Figure 10 compares pressure perturbation profiles across the boundary layer at two locations, $x^* = 249$ mm and $x^* = 359$ mm ($R = 1875.41$ and 2251.88), for a superimposed mode S and mode F. The two locations are upstream and downstream of the synchronization point ($x^* = 0.33184$ m), respectively. The figure shows significant difference between pressure perturbation profiles at $x^* = 249$ mm ($R = 1875.41$). However, pressure perturbation profiles have a good agreement at $x^* = 359$ mm ($R = 2251.88$). This figure confirms that mode F converts to mode S after the synchronization point.

In Figs. 8 and 9, there are very big oscillations of the values of growth rate and phase velocity before the synchronization point. These strong oscillations are a result of the coexistence of mode F, mode S, acoustic waves, and entropy/vorticity waves in the boundary layer. As shown in Figs. 5 and 6, the imposed disturbances are not exactly single boundary-layer waves because of the nonparallel effect; they are only dominated by mode S or mode F. Furthermore, the resonances between different waves enhance such oscillations. After the synchronization point, mode S grows rapidly and becomes the dominant wave in the boundary layer. Therefore, oscillations of growth rate and phase velocity disappear after the synchronization point.

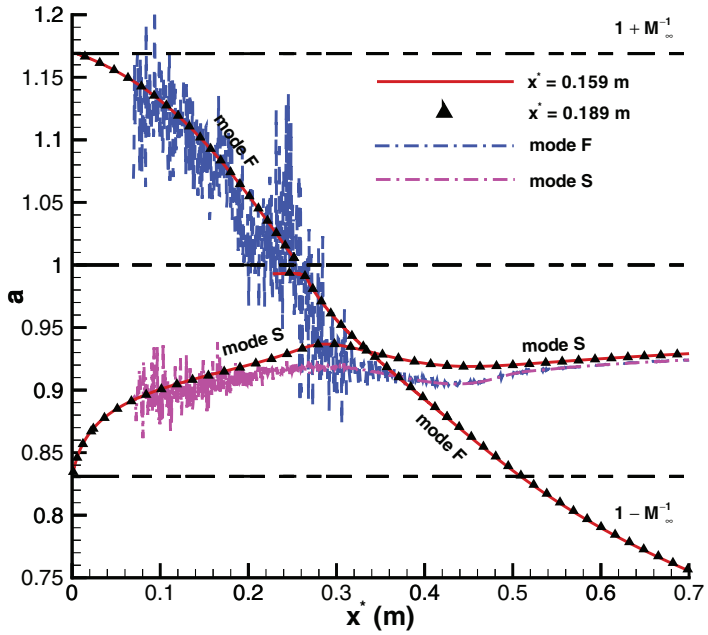

FIG. 9. Comparison of the phase velocity calculated from stability simulations with that obtained from LST for superimposed mode S and mode F.

V. EFFECT OF POROUS COATING ON MODE S

At step 2 of the stability simulations, felt-metal porous coatings, modeled by wall blowing-suction related to pressure oscillation, are used downstream of the superimposed wave. To investigate the role of the synchronization point on boundary layer stabilization, porous coatings are located both upstream and downstream of the synchronization point.

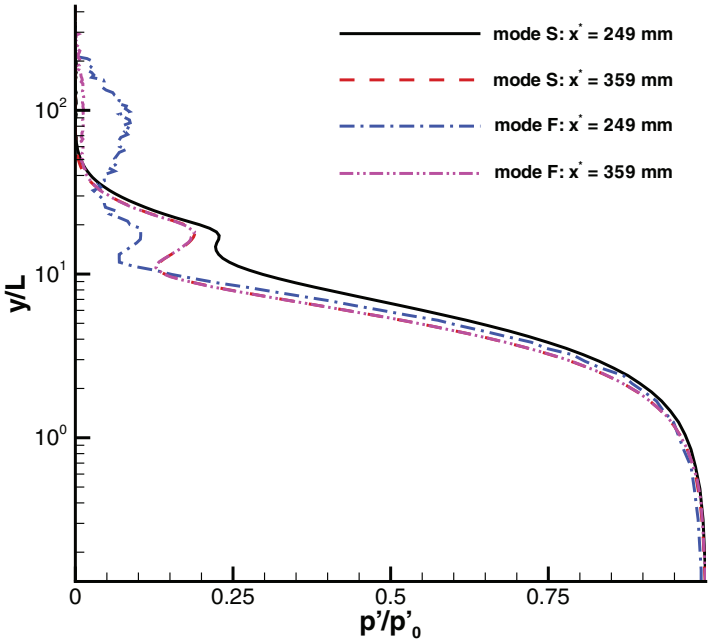

FIG. 10. Comparison of pressure perturbation profiles across the boundary layer at two locations for superimposed mode S and mode F.

TABLE I. Locations of the six sections of porous coating for superimposed mode S and mode F.

Index	x^*_{Start}(mm)	x^*_{End}(mm)	x^*_{Center}(mm)
1	73.5	124.8	99.2
2	193.5	244.8	219.2
3	283.5	304.8	294.2
4	366.5	402.8	384.6
5	466.5	502.8	484.6
6	574.0	645.0	609.5

Parameters of felt-metal porous coating are the same as those used in Fedorov *et al.*'s paper,[11] i.e.,

$$\phi = 0.75, \qquad h^* = 0.75 \text{ mm},$$
$$a_\infty = 1, \qquad d^* = 30\ \mu\text{m},$$
$$\sigma^* = 1.66 \times 10^5 \text{ kg m}^3\text{s}^{-1}, \qquad \gamma = 1.4,$$

where d^* is the fiber diameter, which is related to the characteristic pore size as follows:

$$r_p^* = \frac{\pi d^*}{2 - 3\phi + \phi^2}. \tag{36}$$

For superimposed mode S, six sections of porous coating are considered, with three of them being located upstream of the synchronization point. The locations of porous coatings are listed in Table I. Figure 11 schematically shows porous coating locations for the stability simulations of superimposed mode S. The first three porous coatings are located upstream of the synchronization point whereas the other three are located downstream of the synchronization point. The contours show pressure perturbation excited by superimposed mode S without porous coating. The structures of pressure perturbation contour show that the synchronization point is the location where the first mode converts to the second mode.

To study the effect of porous coating and its location on mode S, a series of stability simulations have been carried out. Specifically, six cases of simulations are considered by adding porous coatings one by one from upstream to downstream. For example, only the first porous coating is used in the first case. The first two porous coatings are used in the second case. Eventually, in the sixth case, all six porous coatings are used. Figure 12 shows pressure perturbations along the flat plate for the six cases of stability simulations, together with the spatial development of mode S without porous coating. It is noticed that pressure perturbations of all six cases with porous coating have a similar

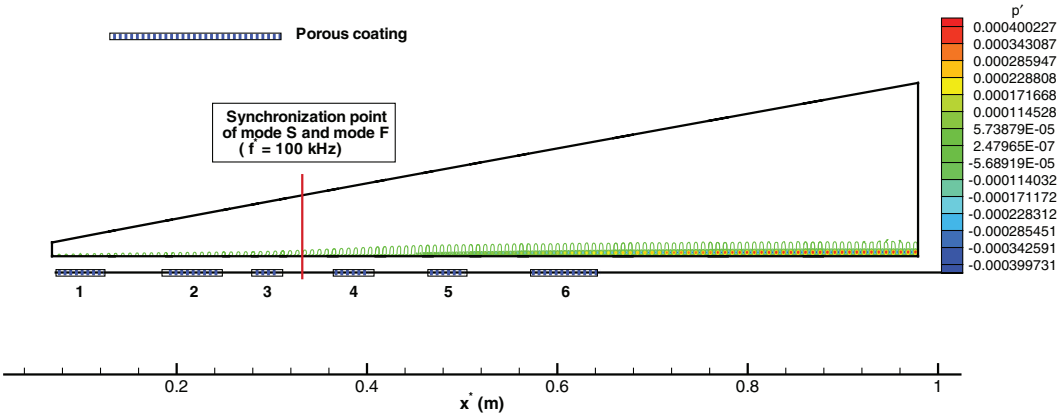

FIG. 11. A schematic of porous coating locations for the stability simulations of superimposed mode S.

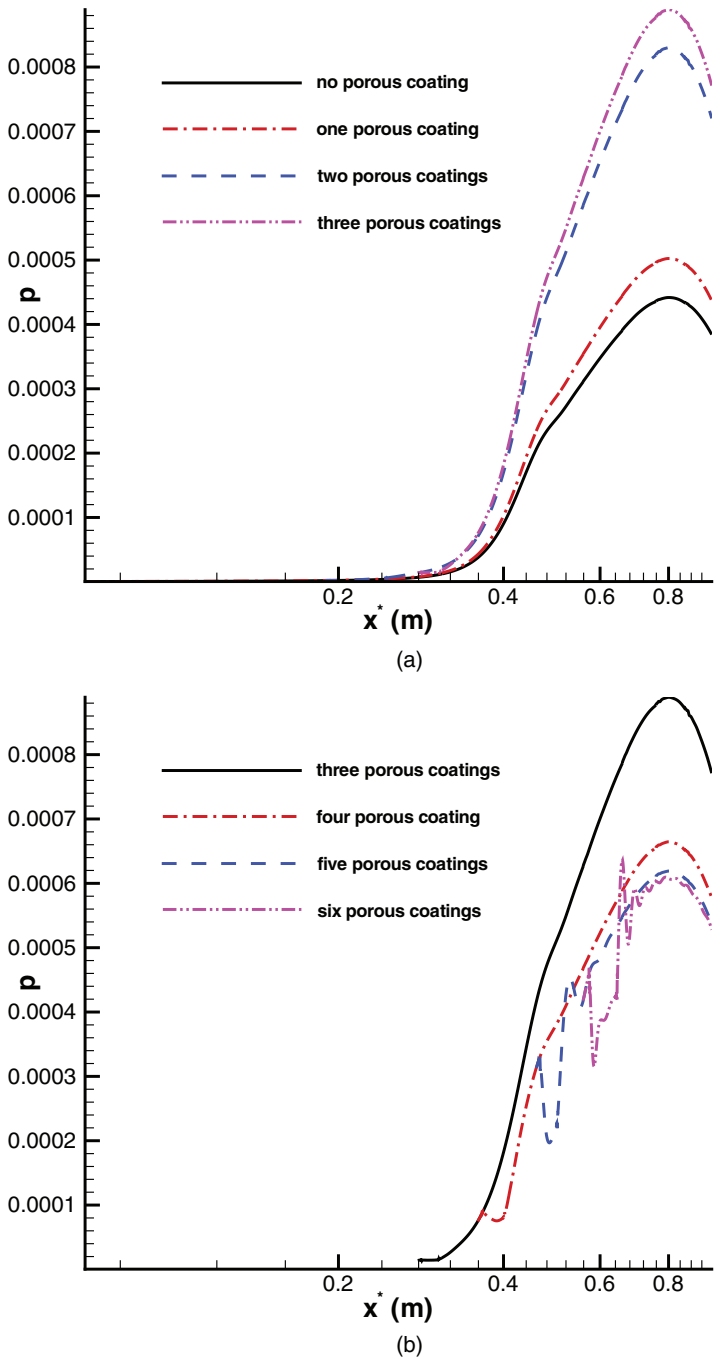

FIG. 12. Comparisons of pressure perturbation along the flat plate for the six cases of stability simulations of superimposed mode S.

profile as that of purely mode S without porous coating with an amplitude peak around $x^* = 0.8$ m ($R = 3361.57$). However, porous coating does affect the amplitude of pressure perturbation.

Porous coatings with the index number from 1 to 3 are upstream of the synchronization point. Figure 12(a) shows that pressure perturbation amplitude increases with the number of porous coatings increasing. When porous coatings with the index number from 4 to 6 are added downstream of the synchronization point, Fig. 12(b) shows that pressure perturbation amplitude decreases with the number of porous coatings increasing. Figure 12 indicates that porous coating destabilizes Mack's

first mode and stabilizes Mack's second mode because the synchronization point is the location where the first mode converts to the second mode. These results are consistent with those of Fedorov *et al.*'s experimental and theoretical study[11] and Maslov's experiments.[15] In order to delay boundary layer transition, it is very important to put porous coating downstream of the synchronization point, where mode S corresponds to the second mode.

In our simulations, porous coatings are not continuous on the flat plate. There are junctures between solid and porous surface at the leading and trailing edges of porous coating. Figures 11 and 12(b) show that the relaxation length of pressure perturbation near the edges of porous coatings is approximately two times the wavelength of the second mode. Therefore, the end effects are local and are neglected in considering the stabilization using porous coating. Similar treatment has been applied in Egorov *et al.*'s numerical simulations.[21]

In Egorov *et al.*'s numerical simulations on the receptivity of a Mach 6 boundary layer over a flat plate with porous coating,[21] porous coating was found to slightly destabilize the first mode and stabilize the second mode. Eventually, porous coating led to a smaller peak amplitude of mode S. In our simulations, all the six cases of stability simulations show a larger peak amplitude of mode S, which means destabilization of the first mode is not slight but quite significant. The difference between two sets of simulation results probably arises from the following three factors. First, different porous coatings are used. In Egorov *et al.*'s simulation regular porous coating was used. Whereas in our simulation, felt-metal porous coating is used. It had been shown in Maslov's experiment[15] that felt-metal UAC is much stronger in first mode destabilization than regular structure UAC. Second, initial strength of mode S in the boundary layer is quite different. In Egorov *et al.*'s simulation, mode S was excited by freestream slow acoustic waves. Due to the receptivity process, only a small portion of boundary layer disturbances are mode S. As a result, destabilization of the first mode might be attenuated by stabilization of the coexistent mode F and continuous waves. In our simulation, mode S is directly superimposed on the boundary layer, and the effects of mode F and continuous waves are left out. Third, the frequency of disturbances is different, which may affect the instability of the first mode.

Figure 13 shows amplification ratios of pressure perturbation peak amplitude for the six cases of stability simulations of superimposed mode S. In this figure, amplification (Ap) and relative amplification (Rap) of pressure perturbation are calculated according to the following formulas:

$$\mathrm{Ap} = (p_i - p_0)/p_0 * 100\% \quad (i = 1, 2, 3, 4, 5, 6)\,, \tag{37}$$

$$\mathrm{Rap} = (p_i - p_{i-1})/p_{i-1} * 100\% \quad (i = 1, 2, 3, 4, 5, 6)\,, \tag{38}$$

where the subscript "0" stands for the spatial development of mode S without porous coating. In Fig. 13(a), number "*i*" stands for the *i*th case of stability simulation using "*i*" porous coatings. In Fig. 13(b), index "*i*" stands for the *i*th porous coating. According to the above definitions, it is clear that, for a specific number *i* in Fig. 13(a), amplification ratio stands for the effect of all the *i* porous coatings used in the stability simulation. For a specific index *i* in Fig. 13(b), relative amplification ratio stands for the effect of *i*th porous coating only. Figure 13 shows that porous coating amplifies the pressure perturbation in all the six cases of stability simulations. For porous coatings with the index from 1 to 3, located upstream of the synchronization point, relative amplification ratios are positive. The other three porous coatings are downstream of the synchronization point, and their relative amplification ratios are negative.

These results indicate that the synchronization point plays an important role on boundary layer stabilization. Disturbances are destabilized or stabilized when porous coating is located upstream or downstream of the synchronization point. It is also shown in Fig. 13(b) that the second porous coating is most efficient in first-mode destabilization whereas the fourth porous coating is most efficient in second-mode stabilization.

Figure 14 compares the growth rate calculated from stability simulations with that obtained from LST for superimposed mode S. The growth rates of stability simulations with porous coating are quite similar to that of purely mode S without porous coating. They all have a good agreement with that of LST in the region from $\omega = 0.11$ to $\omega = 0.13$. When ω is larger than 0.13, mode S

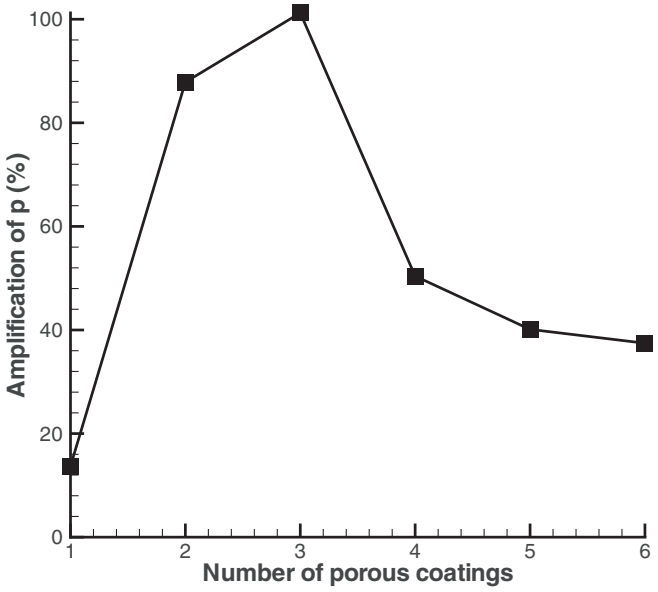

(a)

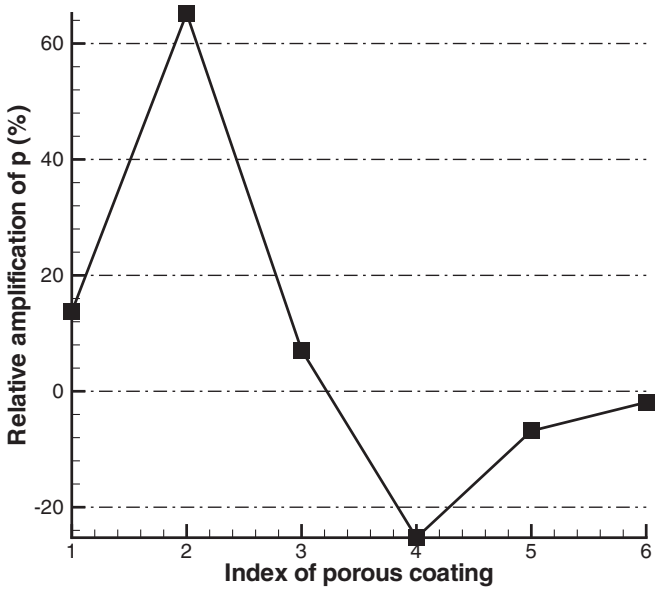

(b)

FIG. 13. Amplification ratio of pressure perturbation peak amplitude for the six cases of stability simulations of superimposed mode S.

obtained by stability simulation becomes more stable than that predicted by LST. However, when ω is smaller than 0.11, mode S obtained by stability simulation becomes more unstable than that predicted by LST. Figure 15 compares the phase velocity calculated from stability simulations with that obtained from LST for superimposed mode S. The phase velocity of stability simulations has a good agreement with that of LST. In regions where porous coating are used, the growth rate and phase velocity calculated from stability simulations are quite different from their counterparts obtained from LST. These two figures show that porous coating only has a local effect on the spatial development of superimposed mode S.

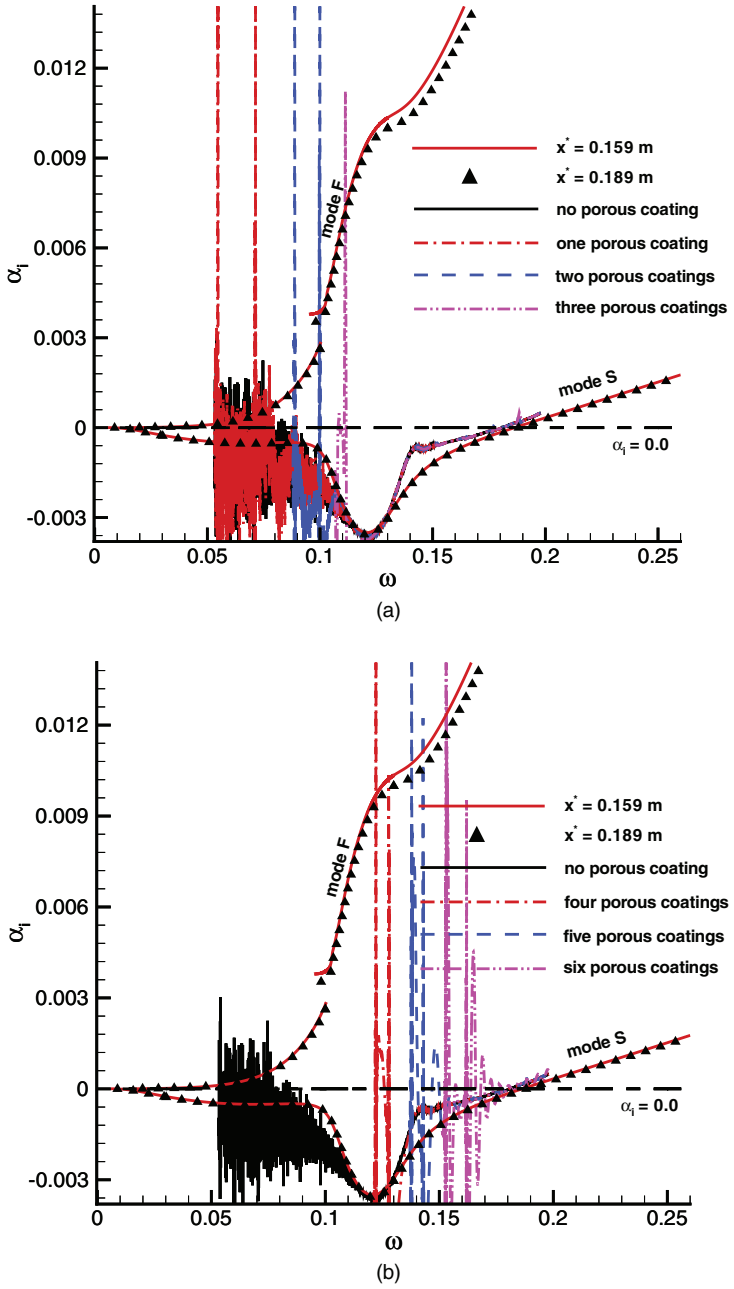

FIG. 14. Comparison of the growth rate calculated from stability simulations with that obtained from LST for superimposed mode S.

VI. EFFECT OF POROUS COATING ON MODE F

In this section, stability simulations are carried out to investigate the effect of porous coating and its location on superimposed mode F. Since mode F converts to mode S after the synchronization point, only the first three sections of porous coating listed in Table I are considered, i.e., only porous coatings upstream of the synchronization point are used. Figure 16 schematically shows porous coating locations for the stability simulations of superimposed mode F. The contours show pressure perturbation excited by superimposed mode F without porous coating. The structures of pressure perturbation contour confirm that all three porous coatings are located upstream of the synchronization point where the second mode does not exist. This figure also shows that mode F

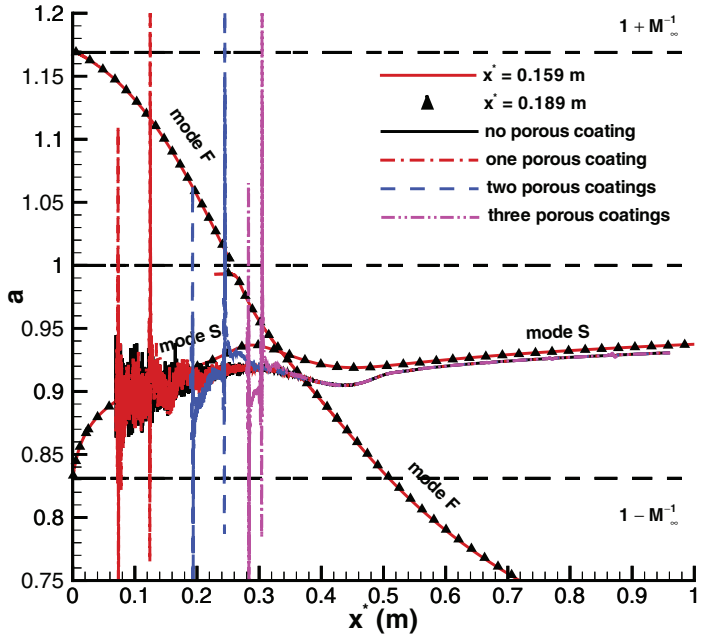

(a)

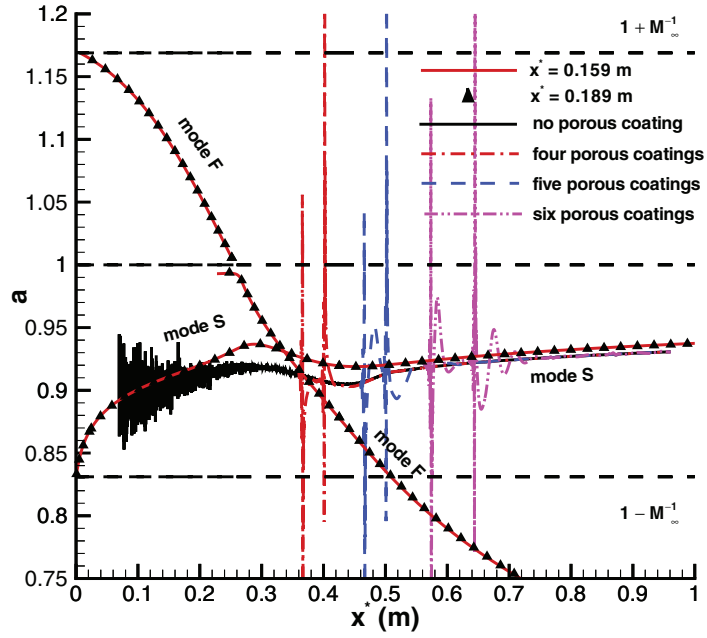

(b)

FIG. 15. Comparison of the phase velocity calculated from stability simulations with that obtained from LST for superimposed mode S.

excites significant acoustic waves outside of the boundary layer, which is quite different from the pressure perturbation contours excited by mode S as shown in Fig. 11.

Specifically, three cases of stability simulations are carried out by adding porous coatings one by one from upstream to downstream. Figure 17 shows pressure perturbations along the flat plate for the three cases of stability simulations of superimposed mode F. It is noticed that porous coating increases pressure perturbation amplitude far downstream of the porous region. The pressure perturbation amplitude increases with an increasing number of porous coatings.

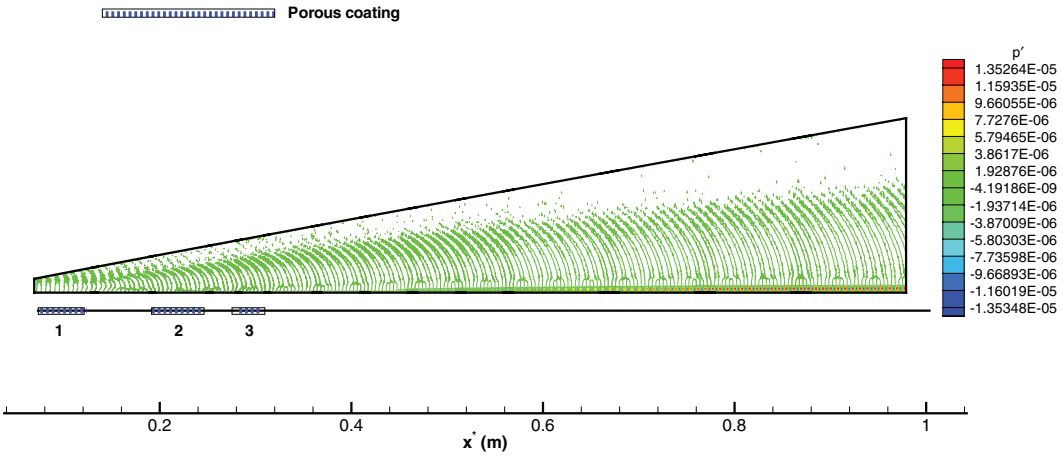

FIG. 16. A schematic of porous coating locations for the stability simulations of superimposed mode F.

To show clearly the spatial development of mode F in porous regions, Fig. 18 compares pressure perturbation amplitude for superimposed mode F obtained from stability simulations with and without porous coating. This figure shows that the effect of porous coating on mode F in porous regions depends on the location of porous coating. For porous coating located in the region (73.5, 124.8) mm, pressure perturbation amplitude decreases in the whole region as shown in Fig. 18(a). Similar phenomenon is observed for porous coating located in the region (283.5, 304.8) mm (Fig. 18(c)). However, for porous coating located in the region (193.5, 244.8) mm, pressure perturbation amplitude decreases initially then increases near the trailing edge of the porous region as shown in Fig. 18(b). As has been mentioned, the increase of mode F at $x^* = 0.24$ m ($R = 1841.21$) is caused by the resonance of mode F with vorticity and entropy waves. This figure also shows that the effects of junctures between solid and porous surfaces at the leading and trailing edges of porous coatings are local. These results indicate that porous coating generally decreases pressure perturbation in porous regions, i.e., porous coating stabilizes mode F in porous regions.

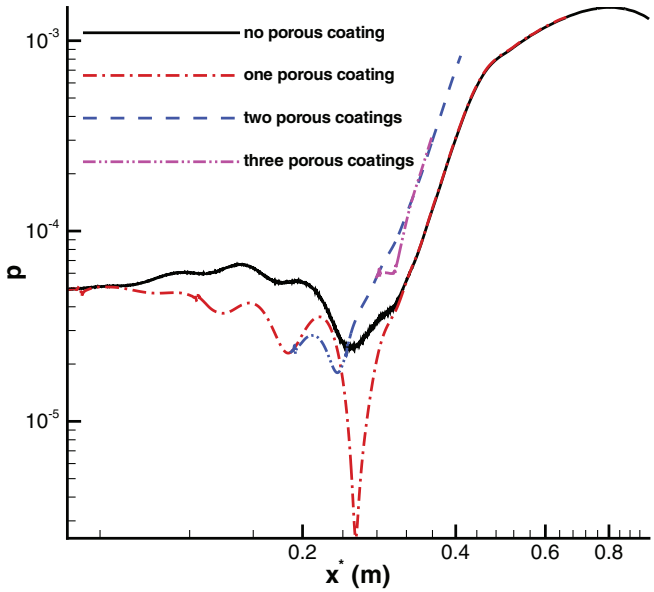

FIG. 17. Comparisons of pressure perturbation along the flat plate for the three cases of stability simulations of superimposed mode F.

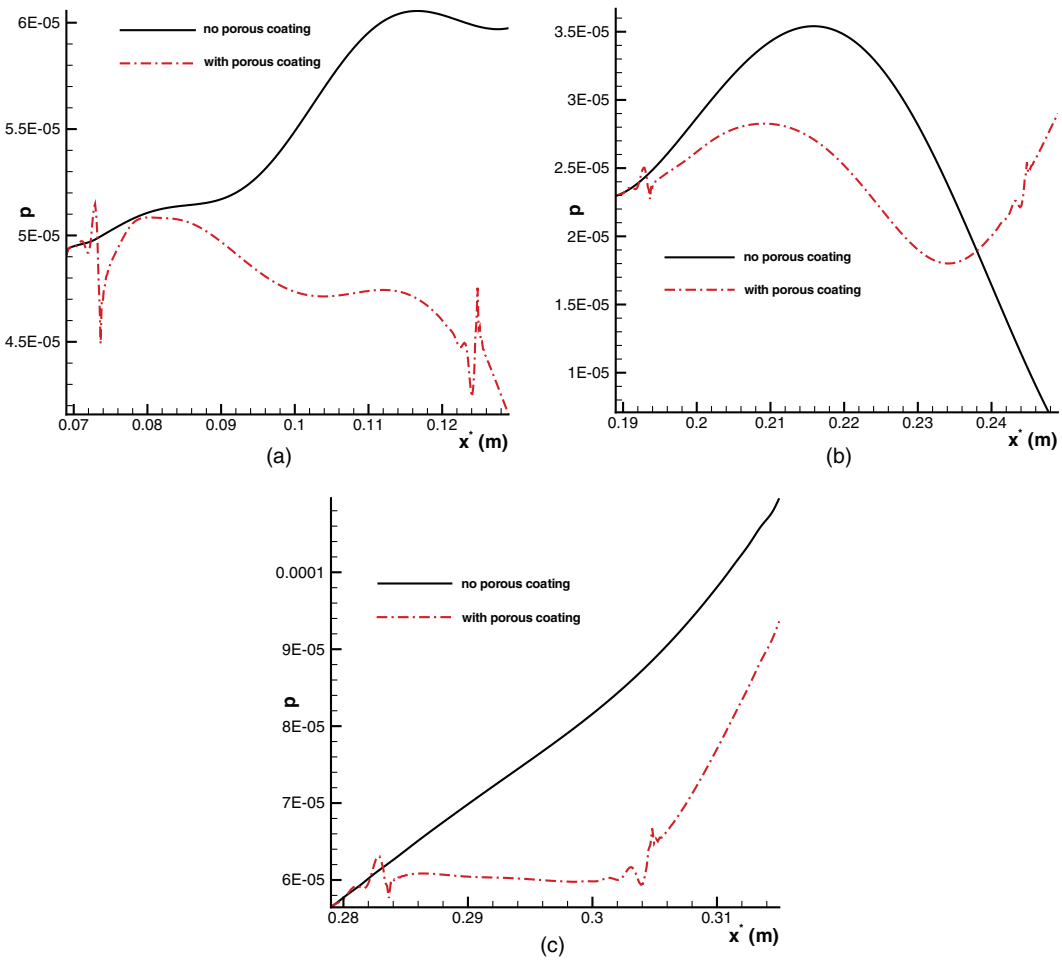

FIG. 18. Comparison of pressure perturbation for superimposed mode F obtained from stability simulations with or without porous coating.

Figure 19 compares the growth rate calculated from stability simulations with that obtained from LST for superimposed mode F. The growth rates of stability simulations with porous coating are quite similar to that of purely mode F without porous coating. All results show that mode F converts to mode S near the synchronization point. After the conversion, the growth rate of stability simulations has a good agreement with that of LST for mode S. Figure 20 compares the phase velocity calculated from stability simulations with that obtained from LST for superimposed mode F. It is clearly shown that the phase velocity of mode F calculated from stability simulations initially follows that obtained from LST. Then mode F converts to mode S around $x^* = 0.32$ m ($R = 2126.04$). The agreement of the two sets of phase velocities downstream of $x^* = 0.30$ m ($R = 2058.53$) confirms that mode S is the dominant wave in the boundary layer. Again, these two figures show that porous coating only has a local effect on mode F.

VII. STABILIZATION OF THE BOUNDARY LAYER DISTURBED BY ONE BLOWING-SUCTION ACTUATOR

Based on the stability simulations for superimposed mode S and mode F, the synchronization point plays an important role in boundary layer stabilization using porous coatings. An efficient way for boundary layer stabilization is to put porous coating downstream of the synchronization point. In this section, stabilization of the boundary layer disturbed by more realistic disturbances is considered. A blowing-suction actuator at the frequency of 100 kHz or 150 kHz is used to excite

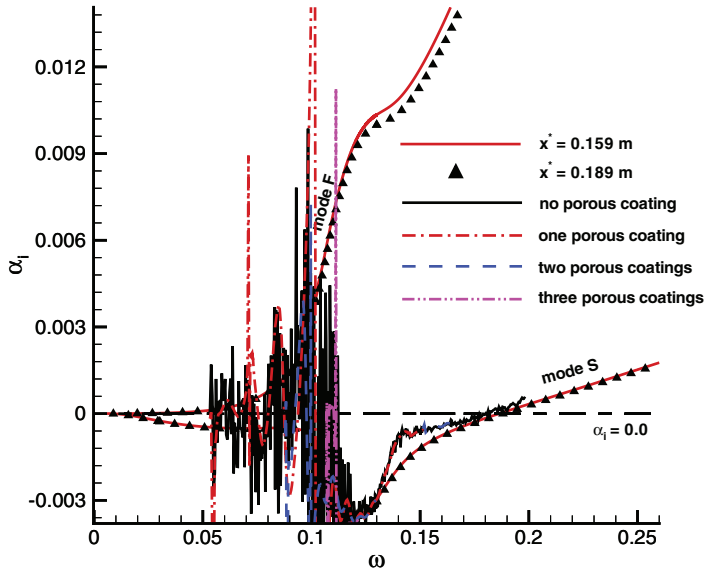

FIG. 19. Comparison of the growth rate calculated from stability simulations with that obtained from LST for superimposed mode F.

boundary layer waves. The model of wall blowing-suction is given in Eq. (25). This study focuses on linear responses of the boundary layer to wall blowing-suction. Therefore, the amplitude of mass flux oscillation is small enough to preserve the linear properties of the disturbances. The dimensionless amplitude coefficient, ϵ_2 in Eq. (25), is given as

$$\epsilon_2 = 1.0 \times 10^{-5} . \tag{39}$$

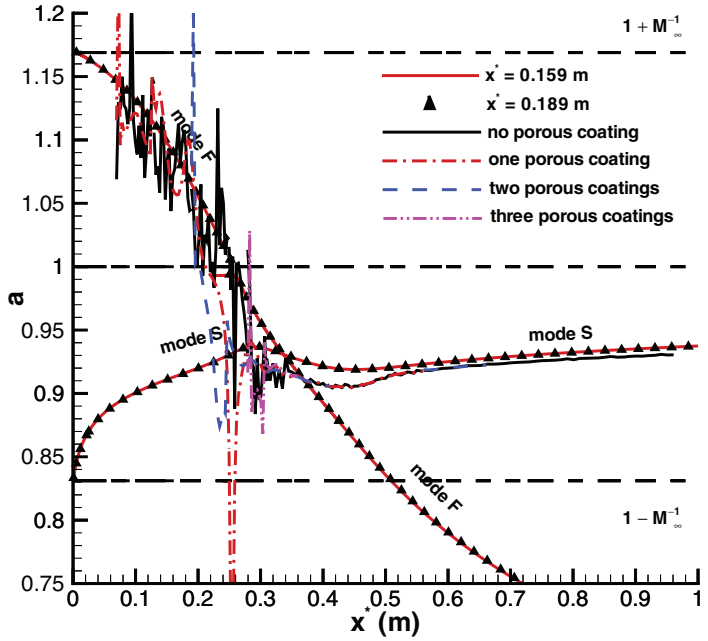

FIG. 20. Comparison of the phase velocity calculated from stability simulations with that obtained from LST for superimposed mode F.

TABLE II. Locations of the three sections of porous coating for stabilization of the boundary layer disturbed by blowing-suction at 100 kHz.

Index	x^*_{Start}(mm)	x^*_{End}(mm)	x^*_{Center}(mm)
1	283.5	304.8	294.2
2	366.5	402.0	383.2
3	316.5	347.0	331.8

The leading and trailing edges of the blowing-suction actuator are located at $x^*_i = 33$ mm and $x^*_e = 37$ mm ($R = 654.98$ and 693.54), respectively.

After the excitation of boundary layer waves, porous coating is used near the synchronization point to stabilize the boundary layer. Specifically, four cases of stability simulations are considered: case 1, without porous coating; case 2, porous coating located upstream of the synchronization point; case 3, porous coating located downstream of the synchronization point; and case 4, porous coating located both upstream and downstream of the synchronization point. The locations of the three sections of porous coating used in cases 2–4 are listed in Table II for blowing-suction at 100 kHz and Table III for blowing-suction at 150 kHz .

Figure 21 shows a schematic of the stabilization of the boundary layer disturbed by wall blowing-suction using porous coating. At the frequency of 100 kHz, the synchronization point is located at 0.33184 m. While at the frequency of 150 kHz, the synchronization point is located at 0.14748 m. Therefore, the first and second porous coatings are located upstream and downstream of the synchronization point, respectively. The third porous coating is located both upstream and downstream of the synchronization point.

Figure 22 compares pressure perturbation amplitudes along the flat plate for the four cases of stability simulations where the boundary layer is disturbed by blowing-suction at 100 kHz. This figure shows that pressure perturbation decreases in porous coating regions. The magnitude of pressure perturbation decrease becomes larger with the location of porous coating moving downstream. However, pressure perturbation of case 2 increases faster than other cases and has the strongest amplitude at $x^* = 0.5$ m ($R = 2657.55$). Pressure perturbation of case 4 has a larger amplitude than that of case 3 and a smaller amplitude than that of case 1. The fact that pressure perturbation of case 2 has the largest amplitude indicates that mode S has the strongest amplitude for this case.

In case 2, porous coating is located upstream of the synchronization point, where mode S corresponds to the first mode. In cases 3 and 4, porous coating is totally or partially located downstream of the synchronization point, where mode S corresponds to the second mode. The difference of pressure perturbation amplitudes among the four cases can generally be explained by the conclusion drawn from the stability simulations of superimposed mode S and mode F: disturbances are destabilized when porous coating is located upstream of the synchronization point and stabilized when porous coating is downstream of the synchronization point.

Here is more explanation for case 2. Although porous coating destabilizes the first mode, the coexistent mode F and continuous waves induced by wall blowing-suction are stabilized. As a result, pressure perturbation decreases in porous coating region. The destabilization of the first mode is proved by the fast increase of pressure perturbation downstream. Figure 22 shows that at the location

TABLE III. Locations of the three sections of porous coating for stabilization of the boundary layer disturbed by blowing-suction at 150 kHz.

Index	x^*_{Start}(mm)	x^*_{End}(mm)	x^*_{Center}(mm)
1	73.5	124.8	99.2
2	193.5	244.8	219.2
3	132.3	165.6	149.0

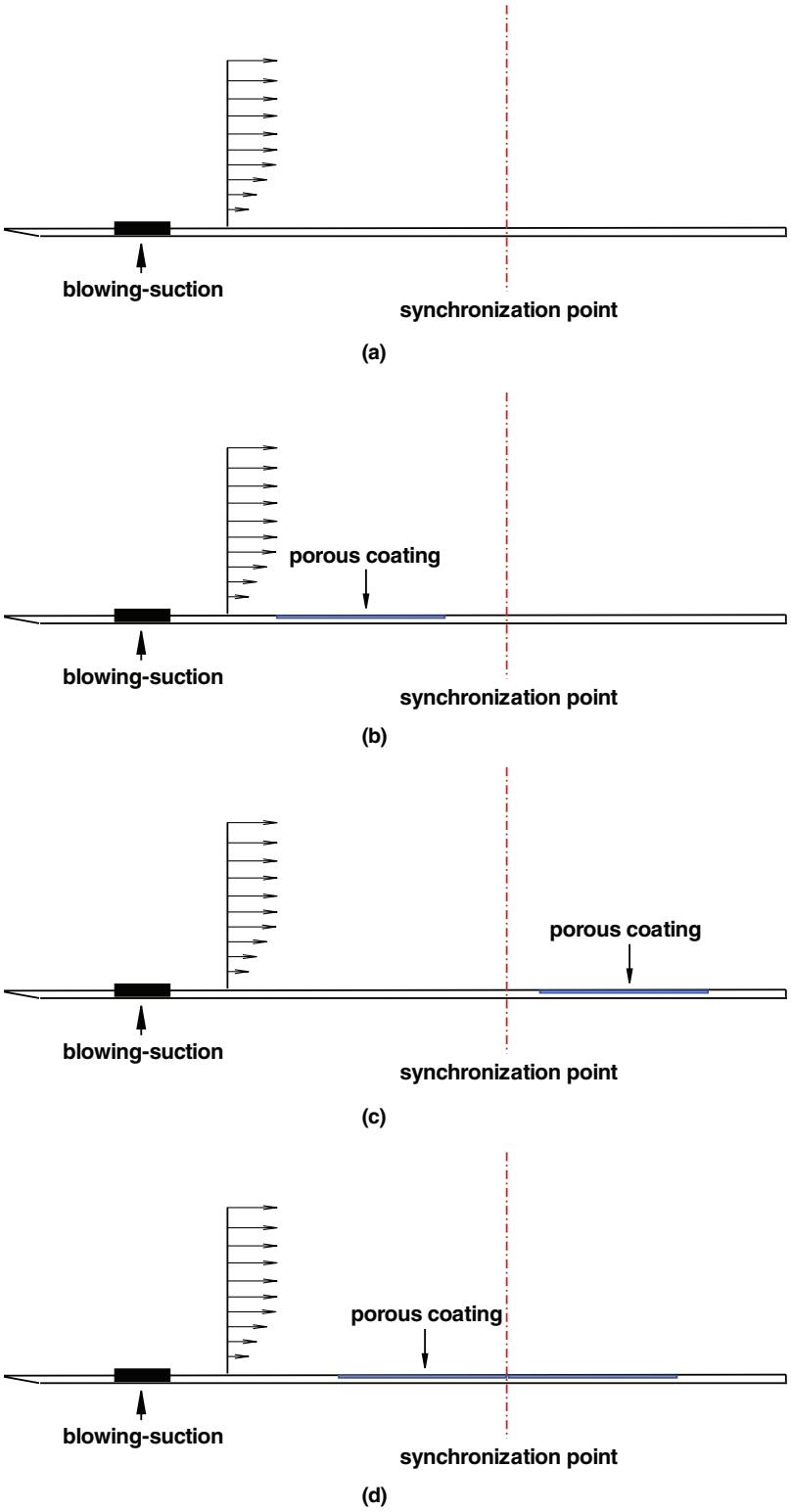

FIG. 21. A schematic of stabilizations of the boundary layer disturbed by wall blowing-suction using porous coating: (a) case 1, (b) case 2, (c) case 3, and (d) case 4.

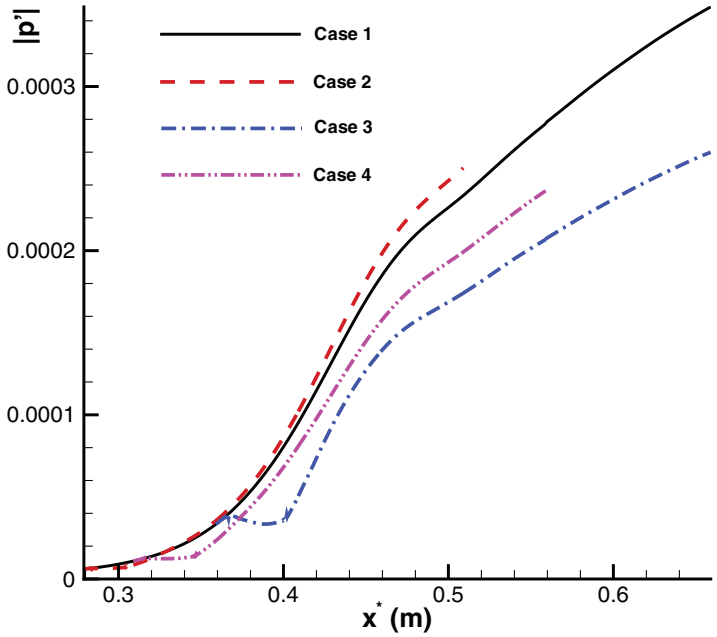

FIG. 22. Pressure perturbation amplitudes along the flat plate for the stabilization of the boundary layer disturbed by blowing-suction at 100 kHz using porous coating.

of $x^* = 0.66$ m ($R = 3053.30$), a 25% decrease of pressure perturbation amplitude is achieved when porous coating is located downstream of the synchronization point (case 3).

Figure 23 compares pressure perturbation amplitudes along the flat plate for the four cases of stability simulations where the boundary layer is disturbed by blowing-suction at 150 kHz. This figure also shows that pressure perturbation decreases in porous coating regions. However, the magnitude of pressure perturbation decrease is quite large in case 2 where porous coating is upstream of the synchronization point. This result is fairly different from that shown in Fig. 22. At

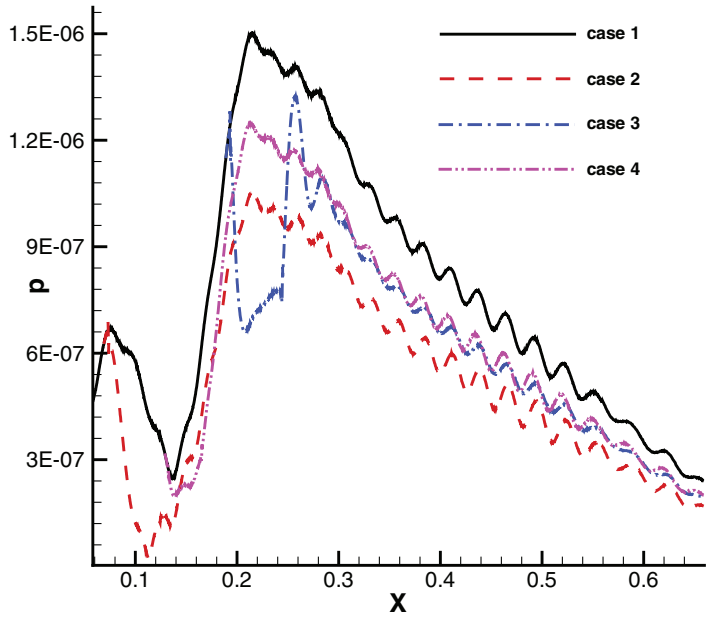

FIG. 23. Pressure perturbation amplitudes along the flat plate for the stabilization of the boundary layer disturbed by blowing-suction at 150 kHz using porous coating.

the frequency of 150 kHz, the synchronization point is closer to the blowing-suction actuator than that at the frequency of 100 kHz. As a result, the effects of coexistent mode F and continuous waves induced by wall blowing-suction are more significant. It is the coexisting mode F and continuous waves that cause the decrease of pressure perturbation around $x^* = 0.1$ m in case 1 where no porous coating is used. The strong coexistent mode F and continuous waves make complex the stabilization of the boundary layer. Fortunately, the results of cases 3 and 4 still show that porous coating is more efficient in the boundary-layer stabilization if it is downstream of the synchronization point.

The numerical results show that the synchronization point plays an important role in the stabilization of the hypersonic boundary layer using porous coating. The most efficient way to stabilize the boundary layer is to put porous coating downstream of the synchronization point.

VIII. CONCLUSION

The stabilization of a Mach 5.92 boundary layer over a flat plate using local sections of porous coating is studied by a combination of direct numerical simulation and linear stability theory. The emphasis of this paper is on the effect of porous coating location and the destabilization of Mack's first mode. Numerical simulation results are interpreted by comparing with LST analyses.

At first, the role of the synchronization point on boundary layer stabilization is investigated. A series of stability simulations are carried out by putting porous coatings both upstream and downstream of the synchronization point. The results show that porous coating only has a local effect on the spatial development of superimposed mode S or mode F. In the case of mode S, porous coating destabilizes Mack's first mode and stabilizes Mack's second mode. In the case of mode F, porous coating generally has a stabilizing effect. When propagating downstream, mode F converts to mode S near the synchronization point.

It is found that the synchronization point plays an important role in the stabilization of the hypersonic boundary layer using porous coating. Disturbances are destabilized when porous coating is located upstream of the synchronization point and stabilized when porous coating is downstream of the synchronization point. For felt-metal porous coating, the destabilization of Mack's first mode is significant. The results suggest that an efficient way to stabilize hypersonic boundary layers is to put porous coating downstream of the synchronization point.

Finally, porous coating is used to stabilize the boundary layer disturbed by a single-frequency blowing-suction actuator. A 25% decrease in pressure perturbation amplitude is achieved when porous coating is located downstream of the synchronization point, which confirms that putting porous coating downstream of the synchronization point is an efficient way to stabilize boundary-layer flows.

ACKNOWLEDGMENTS

This work was sponsored by the AFOSR/NASA National Center for Hypersonic Research in Laminar-Turbulent Transition and by the Air Force Office of Scientific Research, USAF, under Grant Nos. FA9550-07-1-0414 and FA9550-04-1-0029, monitored by Dr. John Schmisseur. The views and conclusions contained herein are those of the authors and should not be interpreted as necessarily representing the official policies or endorsements either expressed or implied, of the Air Force Office of Scientific Research or the U.S. Government.

[1] United States Defense Science Board, Report of the Defense Science Board Task Force on National Aero-Space Plane (NASP) Program, 1992.
[2] E. Reshotko, "Is Re_θ/Me a meaningful transition criterion?," AIAA J. **45**(7), 1441 (2007).
[3] M. V. Morkovin, E. Reshotko, and T. Herbert, "Transition in open flow systems - a reassessment," Bull. Am. Phys. Soc. **39**, 1882 (1994).
[4] X. Zhong and X. Wang, "Direct numerical simulation on the receptivity, instability, and transition of hypersonic boundary layers," Annu. Rev. Fluid Mech. **44**, 527 (2012).
[5] L. M. Mack, "Linear stability theory and the problem of supersonic boundary-layer transition," AIAA J. **13**(3), 278 (1975).
[6] Y. Ma and X. Zhong, "Receptivity of a supersonic boundary layer over a flat plate. Part 1:Wave structures and interactions," J. Fluid Mech. **488**, 31 (2003).
[7] A. Tumin, "Three-dimensional spatial normal modes in compressible boundary layers," J. Fluid Mech. **586**, 295 (2007).

[8] A. V. Fedorov and A. Tumin, "High-speed boundary-layer instability: old terminology and a new framework," AIAA J. **49**(8), 1647 (2011).
[9] A. V. Fedorov, N. D. Malmuth, A. Rasheed, and H. G. Hornung, "Stabilization of hypersonic boundary layers by porous coatings," AIAA J. **39**(4), 605 (2001).
[10] A. Rasheed, H. G. Hornung, A. V. Fedorov, and N. D. Malmuth, "Experiments on passive hypervelocity boundary-layer control using an ultrasonically absorptive surface," AIAA J. **40**(3), 481 (2002).
[11] A. V. Fedorov, A. N. Shiplyuk, A. A. Maslov, E. V. Burov, and N. D. Malmuth, "Stabilization of a hypersonic boundary layer using an ultrasonically absorptive coating," J. Fluid Mech. **479**, 99 (2003).
[12] A. N. Shiplyuk, E. V. Burov, A. A. Maslov, and V. M. Fomin, "Effect of porous coatings on stability of hypersonic boundary layers," J. Appl. Mech. Tech. Phys. **45**(2), 286 (2004).
[13] A. V. Fedorov, V. F. Kozlov, A. N. Shiplyuk, A. A. Maslov, and N. D. Malmuth, "Stability of hypersonic boundary layer on porous wall with regular microstructure," AIAA J. **44**(8), 1866 (2006).
[14] N. Chokani, D. A. Bountin, A. N. Shiplyuk, and A. A. Maslov, "Nonlinear aspects of hypersonic boundary-layer stability on a porous surface," AIAA J. **43**(1), 149 (2005).
[15] A. A. Maslov, *Stabilization of Hypersonic Boundary Layer by Microstructural Porous Coating*, IUTAM Symposium on One Hundred Years of Boundary Layer Research Vol. 345 (Springer, Netherlands, 2006).
[16] V. F. Kozlov, A. V. Fedorov, and N. D. Malmuth, "Acoustic properties of rarefied gases inside pores of simple geometries," J. Acoust. Soc. Am. **117**(6), 3402 (2005).
[17] A. A. Maslov, A. V. Fedorov, D. A. Bountin, A. N. Shiplyuk, A. A. Sidorenko, N. D. Malmuth, and H. Knauss, "Experimental study of transition in hypersonic boundary layer on ultrasonically absorptive coating with random porosity," AIAA Paper 2008-587, 2008.
[18] A. V. Fedorov, V. F. Kozlov, and R. C. Addison, "Reflection of acoustic disturbances from a porous coating of regular microstructure," AIAA Paper 2008-3902, 2008.
[19] G. A. Bres and T. Colonius, "Three-dimensional instabilities in compressible flow over open cavities," J. Fluid Mech. **599**, 309 (2008).
[20] A. V. Fedorov and N. D. Malmuth, "Parametric studies of hypersonic laminar flow control using a porous coating of regular microstructure," AIAA Paper 2008–588, 2008.
[21] I. V. Egorov, A. V. Fedorov, and V. G. Soudakov, "Receptivity of a hypersonic boundary layer over a flat plate with a porous coating," J. Fluid Mech. **601**, 165 (2008).
[22] N. D. Sandham and H. Lüdeke, "Numerical study of Mach 6 boundary-layer stabilization by means of a porous surface," AIAA J. **47**(9), 2243 (2009).
[23] S. O. Stephen and V. Michael, "Effects of porous walls on hypersonic boundary layer over a sharp cone," AIAA Paper 2010-4286, 2010.
[24] S. V. Lukashevich, A. A. Maslov, A. N. Shiplyuk, A. V. Fedorov, and V. G. Soudakov, "Stabilization of high-speed boundary layer using porous coating of various thickness," AIAA Paper 2010-4720, 2010.
[25] X. Wang, X. Zhong, and Y. Ma, "Response of a hypersonic boundary layer to wall blowing-suction," AIAA J. **49**(7), 1336 (2011).
[26] X. Wang and X. Zhong, "Effect of wall perturbations on the receptivity of a hypersonic boundary layer," Phys. Fluids **21**, 044101 (2009).
[27] A. A. Maslov, A. N. Shiplyuk, A. Sidorenko, and D. Arnal, "Leading-edge receptivity of a hypersonic boundary layer on a flat plate," J. Fluid Mech. **426**, 73 (2001).
[28] X. Wang and X. Zhong, "Receptivity of a hypersonic flat-plate boundary layer to three-dimensional surface roughness," J. Spacecr. Rockets **45**(6), 1165 (2008).
[29] J.-F. Allard and Y. Champoux, "New empirical equations for sound propagation in rigid frame fibrous materials," J. Acoust. Soc. Am. **91**(6), 3346 (1992).
[30] A. Tumin, X. Wang, and X. Zhong, "Direct numerical simulation and the theory of receptivity in a hypersonic boundary layer," Phys. Fluids **19**, 014101 (2007).
[31] A. Tumin, X. Wang, and X. Zhong, "Numerical simulation and theoretical analysis of perturbations in hypersonic boundary layers," AIAA J. **49**(3), 463 (2011).